

Graphene Layers-Wrapped Fe/Fe₅C₂ Nanoparticles Supported on N-doped Graphene Nanosheets for Highly Efficient Oxygen Reduction

Enlai Hu, Xin-Yao Yu, Fang Chen, Yadan Wu, Yong Hu,* and Xiong Wen (David) Lou*

Synthesis of highly efficient nonprecious metal electrocatalysts for the oxygen reduction reaction (ORR) superior to platinum (Pt) is still a big challenge. Herein, a new highly active ORR electrocatalyst is reported based on graphene layers-wrapped Fe/Fe₅C₂ nanoparticles supported on N-doped graphene nanosheets (GL-Fe/Fe₅C₂/NG) through simply annealing a mixture of bulk graphitic carbon nitride (g-C₃N₄) and ferrocene. An interesting exfoliation–denitrogen mechanism underlying the conversion of bulk g-C₃N₄ into N-doped graphene nanosheets is revealed. Owing to the high graphitic degree, optimum N-doping level and sufficient active sites from the graphene layers-wrapped Fe/Fe₅C₂ nanoparticles, the as-prepared GL-Fe/Fe₅C₂/NG electrocatalyst obtained at 800 °C exhibits outstanding ORR activity with a 20 mV more positive half-wave potential than the commercial Pt/C catalyst in 0.1 M KOH solution and a comparable onset potential of 0.98 V. This makes GL-Fe/Fe₅C₂/NG an outstanding electrocatalyst for ORR in alkaline solution.

The oxygen reduction reaction (ORR) is an important process in various electrochemical energy technologies such as fuel cells and metal–air batteries.^[1–7] However, the sluggish ORR kinetics at the cathode greatly limits the practical application of these technologies.^[8,9] Up to now, Pt-based catalysts are considered as the most efficient ORR electrocatalysts with more positive onset and half-wave potential.^[10] Nevertheless, they suffer from high cost and scarcity, low stability, and also the issue of methanol crossover. Therefore, it is very desirable and urgent to develop highly efficient and cost-effective nonprecious

metal catalysts (NPMCs) as alternatives to Pt-based electrocatalysts.

Recently, a variety of NPMCs including nanocarbons,^[11–15] transition metal oxides,^[16] carbides/nitrides, and their composites^[17,18] with high activity and stability for ORR have been developed. Among these NPMCs, nanocarbons are considered as one class of promising ORR electrocatalysts due to their high stability,^[19] and their ORR performances could be improved through doping of heteroatoms, such as N, S, B, and O.^[20–23] In addition, nanocomposites of iron carbides and carbon (Fe₃C/C) have also been reported to be highly active toward ORR and the graphitic layers activated by the encapsulated Fe₃C nanoparticles have been regarded as the main active sites for ORR.^[17,18,24–27] Currently, the phase of the

reported iron carbides catalyst is limited to Fe₃C while other phases such as Fe₅C₂ are rarely explored as ORR electrocatalysts,^[28] and the ORR performance of the reported Fe₅C₂-based catalyst including onset potential and half-wave potential still needs to be improved.^[28] Despite these advances, the development of desired nanocarbon or iron carbide-based electrocatalysts with comparable or even superior performance to commercial Pt/C catalyst is still very challenging.

Graphitic carbon nitride (g-C₃N₄), a metal-free semiconductor with a layered structure similar to graphite, has attracted intensive attention.^[29,30] To obtain larger surface area and more active sites, bulk g-C₃N₄ is usually exfoliated into monolayer or few layers,^[31] typically realized by thermal^[31,32] or liquid exfoliation.^[33,34] As liquid exfoliation always suffers from long-term sonication (10–16 h), thermal exfoliation turns out to be an appropriate choice to destack bulk g-C₃N₄. The mechanism of thermal exfoliation is to break hydrogen bonding in the –NH₂/–NH groups between the polymeric melon unit layers, which is not so stable at high temperature (>500 °C) under air or H₂ condition.^[35] As a nitrogen-rich material, g-C₃N₄ has been also employed to synthesize N-doped carbon materials for ORR.^[36–38] However, the ORR activity of these electrocatalysts is still inferior to that of commercial Pt/C.

Herein, we demonstrate a facile solid-state reaction method for the synthesis of graphene layers-wrapped Fe/Fe₅C₂ nanoparticles supported on N-doped graphene nanosheets (denoted as GL-Fe/Fe₅C₂/NG) simply using bulk g-C₃N₄ and ferrocene as the precursors, as depicted in **Figure 1**. During the reaction,

E. Hu, F. Chen, Y. Wu, Prof. Y. Hu
Key Laboratory of the Ministry of Education for Advanced Catalysis Materials
Department of Chemistry
Zhejiang Normal University
Jinhua 321004, China
E-mail: yonghu@zjnu.edu.cn

Prof. X. Y. Yu, Prof. X. W. Lou
State Key Laboratory of Silicon Materials
School of Materials Science and Engineering
Zhejiang University
Hangzhou 310027, China
E-mail: xwlou@ntu.edu.sg, davidlou88@gmail.com

Prof. X. W. Lou
School of Chemical and Biomedical Engineering
Nanyang Technological University
62 Nanyang Drive, Singapore 637459, Singapore

The ORCID identification number(s) for the author(s) of this article can be found under <https://doi.org/10.1002/aenm.201702476>.

DOI: 10.1002/aenm.201702476

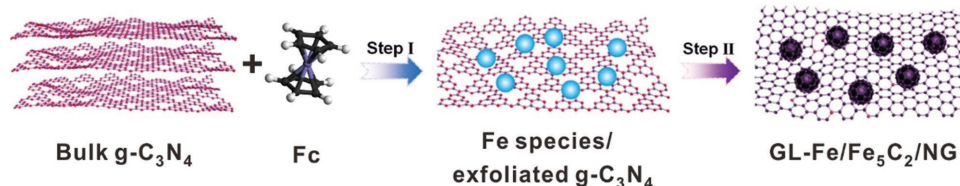


Figure 1. Schematic illustration of the formation of the GL-Fe/ Fe_5C_2 /NG electrocatalyst.

the bulk $g\text{-C}_3\text{N}_4$ is first exfoliated into nanosheets below 650°C and then the exfoliated $g\text{-C}_3\text{N}_4$ nanosheets are transformed into N-doped graphene at temperature above 650°C through a denitrogen reaction. At the same time, graphene layers-wrapped Fe/ Fe_5C_2 nanoparticles are in situ formed on the surface of graphene nanosheets. A series of samples obtained at different temperatures are denoted as GL-Fe/ Fe_5C_2 /NG- T (where T is the heating temperature). The as-prepared GL-Fe/ Fe_5C_2 /NG-800 catalyst possesses favorable characteristics for ORR, including catalytically active composition, porous structure, high specific surface area, optimum N-doping level, as well as high graphitic degree. As expected, the GL-Fe/ Fe_5C_2 /NG-800 catalyst exhibits ORR performance superior to commercial Pt/C with excellent electrocatalytic activity, stability, and methanol tolerance.

Compared to the bulk $g\text{-C}_3\text{N}_4$, the as-prepared GL-Fe/ Fe_5C_2 /NG-800 sample is in a fluffy state (Figure S1, Supporting

Information). The morphology and structure of GL-Fe/ Fe_5C_2 /NG-800 are first examined by scanning electron microscopy (SEM) and transmission electron microscopy (TEM) measurements. As shown in Figure 2a, different from the solid block structure of bulk $g\text{-C}_3\text{N}_4$ (Figure S2, Supporting Information), the product is composed of loose and bushy nanosheets. The TEM images (Figure 2b,c) show that nanoparticles with a size of 20–50 nm are uniformly dispersed on the curved and folded nanosheets. Further high-resolution TEM (HRTEM) measurement (Figure 2d) reveals that these nanoparticles are well wrapped with a few graphene layers with a lattice distance of 0.34 nm, which matches well with the (002) plane of graphite carbon. HRTEM image in Figure 2d discloses that these nanoparticles are well crystallized with an interplanar spacing of 0.21 nm, corresponding to the (021) plane of Fe_5C_2 phase. Powder X-ray diffraction (XRD) measurement indicates the

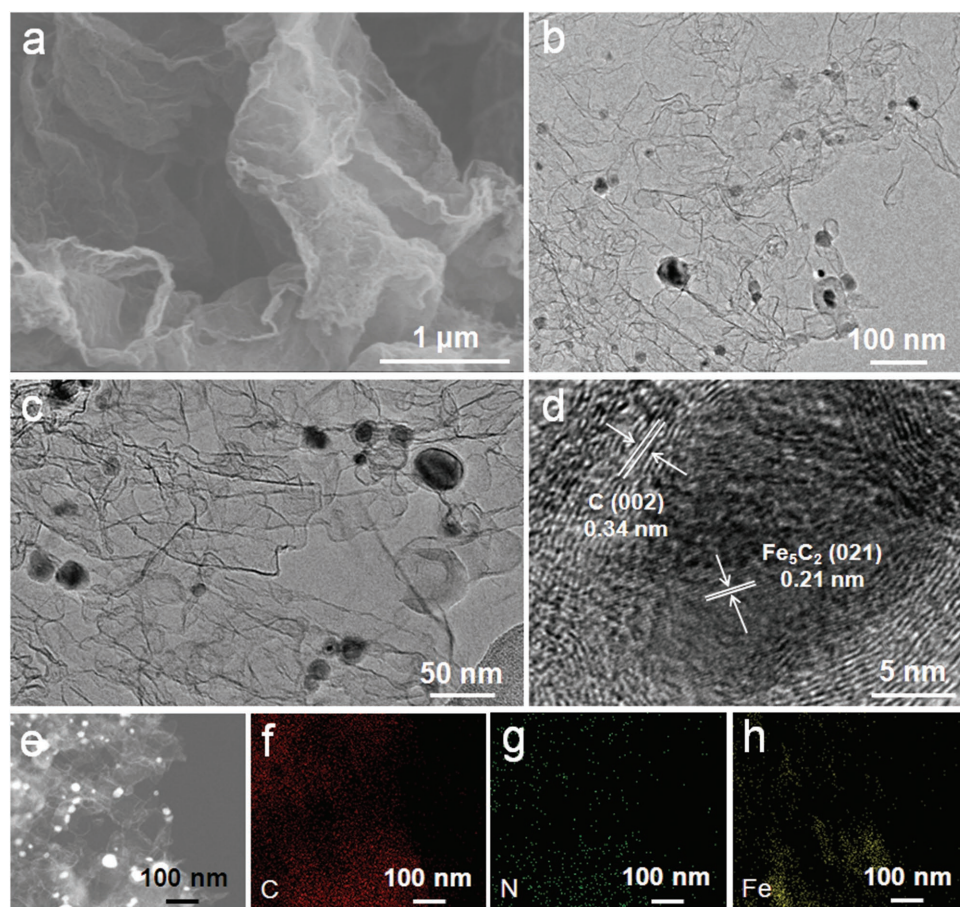


Figure 2. a) SEM image, b,c) TEM images, d) HRTEM image, and e) STEM image of GL-Fe/ Fe_5C_2 /NG-800. f–h) Elemental mapping images of carbon, f) nitrogen, g) and iron h).

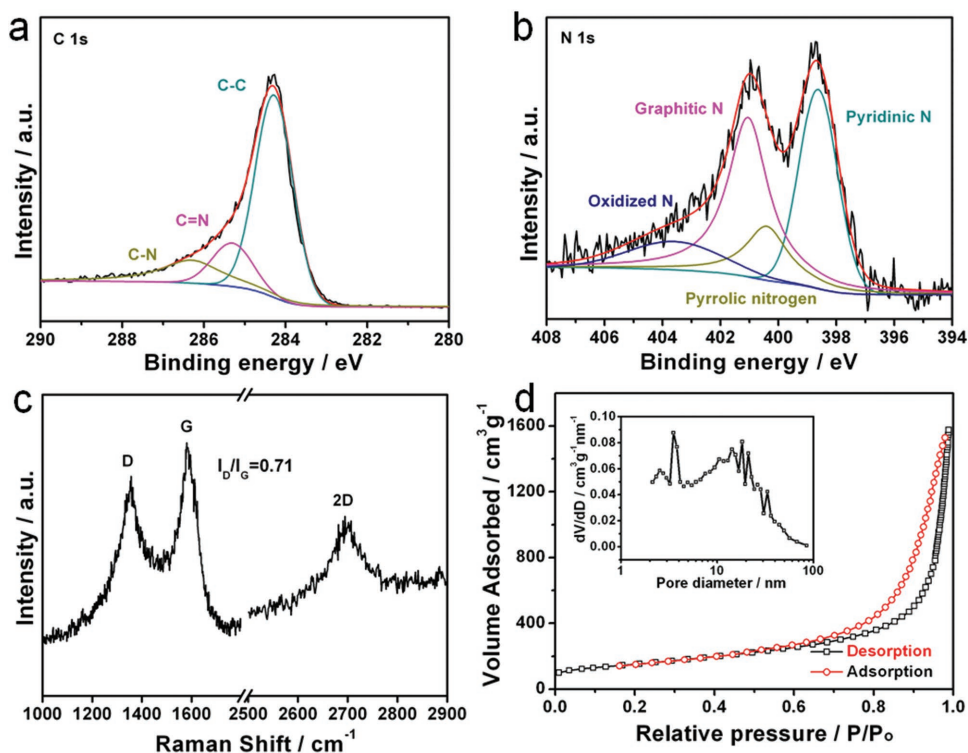


Figure 3. a,b) High-resolution C 1s a) and N 1s b) XPS spectra, c) Raman spectrum, and d) N_2 adsorption–desorption isotherms of GL-Fe/Fe₅C₂/NG-800 and the corresponding pore size distribution (inset).

existence of Fe, Fe₅C₂ as well as graphene in the GL-Fe/Fe₅C₂/NG-800 sample (Figure S3, Supporting Information). The diffraction peak at 26.4° corresponds to the (002) plane of graphene, while the rest of diffraction peaks are from Fe₅C₂ species and α -Fe. The elemental mapping results demonstrate that nitrogen has been successfully doped into the carbon matrix (Figure 2f,g) and the Fe element signals (Figure 2h) mainly exist in the region of nanoparticles (white spots in Figure 2e). The X-ray photoelectron spectroscopy (XPS) survey spectrum of GL-Fe/Fe₅C₂/NG-800 reveals the existence of C (91.96%), N (3.98%), Fe (0.80%), and O (3.26%) elements (Figure S4, Supporting Information). The complex C 1s spectrum is deconvoluted into three main peaks (Figure 3a), corresponding to C–C (284.5 eV), C=N (285.5 eV), and C–N (286.7 eV) bonds,^[39] and the N 1s spectrum (Figure 3b) exhibits four types of nitrogen species, pyridinic N at 398.7 eV, graphitic N at 401.1 eV, pyrrolic N at 400.5 eV, and oxidized N at 403.4 eV.^[40] The high-resolution Fe 2p spectra show the presence of peaks for Fe³⁺ (712.6 and 725.0 eV), Fe²⁺ (710.3 and 723.1 eV), and Fe⁰ (706.8 eV), accompanied by a satellite peak (718.3 eV) (Figure S5, Supporting Information).^[41,42] The presence of graphene is further verified by Raman scattering spectroscopy (Figure 3c). The ratio of D-band (I_D) to G-band (I_G) is 0.71, evidencing the formation of graphene.^[43] The broad 2D peak at 2700 cm⁻¹ implies that the sample is mainly composed of few-layered graphene rather than single-layered graphene.^[44] Figure 3d shows the nitrogen adsorption/desorption isotherm and pore size distribution of GL-Fe/Fe₅C₂/NG-800. The Brunauer–Emmett–Teller (BET) specific surface area, pore volume, and average pore size of GL-Fe/Fe₅C₂/NG-800 are 856 m² g⁻¹, 2.48 cm³ g⁻¹, and 3.5 nm,

respectively. With such high BET specific surface area and pore volume, more active sites and more efficient transport of ORR relevant species can be expected.

The reaction mechanism of ferrocene with g-C₃N₄ is investigated by characterizing the samples obtained at different temperatures using XRD, SEM, Fourier transform-infrared spectroscopy (FT-IR), Raman, and XPS analyses. Compared to the bulk g-C₃N₄, the XRD pattern of GL-Fe/Fe₅C₂/NG-600 changes little with a slight shift of one peak from 27.3° to 27.7° (Figure 4a), indicating the dominance of g-C₃N₄ in GL-Fe/Fe₅C₂/NG-600. The shift of the peak may come from the undulation of the lattice constant during the reaction. The morphology of GL-Fe/Fe₅C₂/NG-600 (Figure S6, Supporting Information) becomes looser than that of the pristine dense and solid g-C₃N₄, demonstrating the exfoliation of g-C₃N₄ at this temperature in the presence of ferrocene. The color of the pristine g-C₃N₄ is yellow while GL-Fe/Fe₅C₂/NG-600 is in dark gray color (Figure S1, Supporting Information). In the GL-Fe/Fe₅C₂/NG-650 sample, the diffraction peaks of g-C₃N₄ disappear and new weak peaks related to carbon and Fe/Fe₅C₂ components at around 25.7°, 43°, and 45° appear (Figure 4a), suggesting the formation of graphitic carbon and Fe/Fe₅C₂ with low crystalline degree. As revealed by the SEM image (Figure S7, Supporting Information), the GL-Fe/Fe₅C₂/NG-650 sample consisting of nanosheets is quite shaggy and the color of the sample is black in a fluffy state (Figure S7b, Supporting Information), which is similar to the GL-Fe/Fe₅C₂/NG-800 sample. In the FT-IR spectra, the strong bands in the range of 1200–1650 cm⁻¹ (stretching modes of CN heterocycles) and the broad peaks in the range of 2988–3340 cm⁻¹ corresponding to the vibration

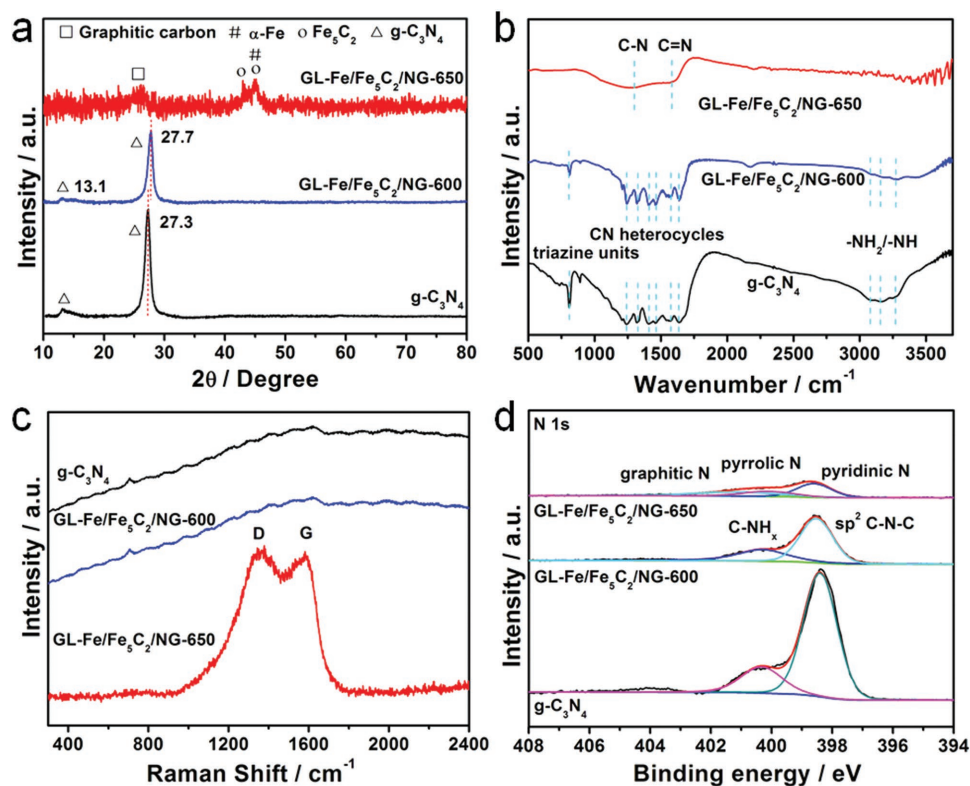


Figure 4. a) XRD patterns, b) FT-IR spectra, c) Raman spectra, and d) high-resolution N 1s spectra of $g\text{-C}_3\text{N}_4$, GL-Fe/Fe₅C₂/NG-600 and GL-Fe/Fe₅C₂/NG-650.

modes of $-\text{NH}_2/-\text{NH}$ groups are more prominent in the $g\text{-C}_3\text{N}_4$ sample. While for GL-Fe/Fe₅C₂/NG-600, these peaks become weaker, suggesting the loss of $-\text{NH}_2/-\text{NH}$ groups at the temperature of 600 °C. Only two main peaks located at about 1600 cm⁻¹ (C=N) and 1300 cm⁻¹ (C-N) are observed in GL-Fe/Fe₅C₂/NG-650, confirming the formation of carbon materials. The Raman spectra in Figure 4c show that the typical D and G bands become remarkable in GL-Fe/Fe₅C₂/NG-650 compared to the other two samples, further evidencing the formation of graphitic carbon. XPS inspection also confirms the denitrogen process. As shown in Figure 4d, the peaks in the N 1s spectra at 400.8, 399.7, and 398.6 eV correspond to C-NH_x (amino functional groups), sp³ H-N-[C]₃, and sp² C-N-C, respectively.^[34] Compared with the N 1s spectra of $g\text{-C}_3\text{N}_4$, the decrease of peak area ratio of C-NH_x in GL-Fe/Fe₅C₂/NG-600 suggests the loss of $-\text{NH}_2/-\text{NH}$ groups. Moreover, the N species in the GL-Fe/Fe₅C₂/NG-650 are assigned to pyridinic N, pyrrolic N, and graphitic N. The decrease of N content (Figure S8, Supporting Information) further confirms the denitrogen process. Based on the above analysis, a possible mechanism for the formation of such catalysts is proposed. Ferrocene will decompose and release gaseous products (H₂, CH₄, C₅H₆, etc.) when treated at a temperature higher than 550 °C,^[45] and the $-\text{NH}_2/-\text{NH}$ groups in $g\text{-C}_3\text{N}_4$ are so unstable that they can be reduced by H₂ without changing the main structure of $g\text{-C}_3\text{N}_4$.^[35] At a temperature below 600 °C, H₂ gas is expected to be released from the decomposition of ferrocene and the released H₂ will react with the $-\text{NH}_2/-\text{NH}$ groups in $g\text{-C}_3\text{N}_4$,

leading to the exfoliation of the $g\text{-C}_3\text{N}_4$.^[35] With the temperature increased to 650 °C, Fe/Fe₅C₂ nanoparticles are generated from the decomposition of ferrocene and $g\text{-C}_3\text{N}_4$ has begun to transform into graphitic carbon with relatively low crystalline degree. When the temperature is higher than 650 °C, the generated Fe/Fe₅C₂ nanoparticles will become more crystallized and most of the N will be removed from the basic structure of $g\text{-C}_3\text{N}_4$ to form N-doped graphene with the help of Fe/Fe₅C₂ nanoparticles, which is similar to the previously reported result.^[46] Meanwhile, graphitic layers are supposed to form on the surface of Fe/Fe₅C₂ nanoparticles with the released hydrocarbon products from ferrocene as carbon source. The release of H₂ from the ferrocene favors the exfoliation of $g\text{-C}_3\text{N}_4$ at temperature below 600 °C, while the in situ generated Fe/Fe₅C₂ nanoparticles promote the growth of N-doped graphene nanosheets and the outer graphene layers around the nanoparticles at temperature higher than 650 °C.

The ORR activity of the GL-Fe/Fe₅C₂/NG-800 catalyst is first evaluated through cyclic voltammetry (CV) measurement. A well-defined cathodic peak centered at 0.85 V (vs reversible hydrogen electrode (RHE)) can be clearly observed when the electrolyte is saturated with O₂ (Figure 5a). This cathodic peak is more positive than that of commercial Pt/C (0.83 V, Figure S9a, Supporting Information), suggesting outstanding ORR catalytic activity of GL-Fe/Fe₅C₂/NG-800. Linear sweep voltammetry (LSV) curves of GL-Fe/Fe₅C₂/NG-800 (Figure 5b) and commercial Pt/C (Figure S9b, Supporting Information) are also recorded through the rotating disk electrode (RDE) setup at

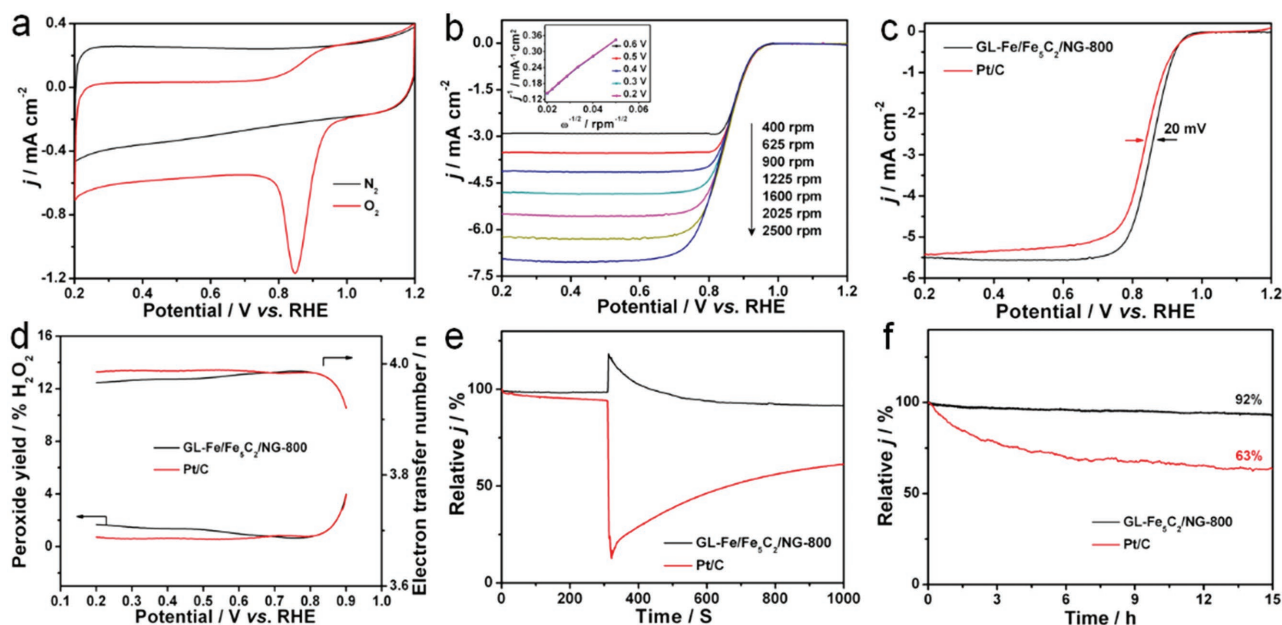


Figure 5. a) CV profiles of the GL-Fe/Fe₅C₂/NG-800 catalyst in 0.1 M KOH solution. b) LSV curves of the GL-Fe/Fe₅C₂/NG-800 catalyst at different rotation speeds. The inset of (b) shows the corresponding K–L plot. c) LSV curves of the Pt/C and GL-Fe/Fe₅C₂/NG-800 catalysts at a rotation speed of 1600 rpm. d) H₂O₂ yield curves and the calculated electron transfer number of the Pt/C and GL-Fe/Fe₅C₂/NG-800 catalysts. e) Chronoamperometric response of the Pt/C and GL-Fe/Fe₅C₂/NG-800 catalysts at 0.6 V in O₂ saturated 0.1 M KOH solution with the addition of 50 mL of methanol. f) Chronoamperometric response of the Pt/C and GL-Fe/Fe₅C₂/NG-800 catalysts at 0.6 V in O₂ saturated 0.1 M KOH solution.

different rotation speeds. Typically, a higher rotating speed with shortened diffusion distance delivers higher current density. Furthermore, the kinetic parameters for electron transfer numbers (n) are analyzed based on the RDE results according to the Koutecky–Levich (K–L) equation (Equations (1) and (2)). The corresponding linearity of K–L plots (inset of Figure 5b) suggests the first-order reaction kinetics toward the concentration of dissolved oxygen and similar electron transfer numbers for ORR at various potentials. The n value of GL-Fe/Fe₅C₂/NG-800 is calculated to be 3.95–3.98 at the potential ranging from 0.2 to 0.7 V, similar to that of commercial Pt/C ($n \approx 4.0$, inset of Figure S9b, Supporting Information), indicating a four-electron pathway of ORR and the direct reduction of O₂ to OH⁻. Prominently, with similar onset potential of 0.98 V, the half-wave potential of GL-Fe/Fe₅C₂/NG-800 is 20 mV more positive than that of the commercial Pt/C ($E_{1/2}$, 0.86 vs 0.84 V in Figure 5c). The ORR activity of GL-Fe/Fe₅C₂/NG-800 is also superior to that of GL-Fe/Fe₅C₂/NG-700 and GL-Fe/Fe₅C₂/NG-900 (Figure S10, Supporting Information). The electrochemical active surface area (ECSA) of GL-Fe/Fe₅C₂/NG-700, GL-Fe/Fe₅C₂/NG-800, and GL-Fe/Fe₅C₂/NG-900 is determined to be 30, 85, and 45 cm², respectively (Figure S11, Supporting Information), further confirming the higher activity of GL-Fe/Fe₅C₂/NG-800. The main reason for the slightly inferior ORR activity of GL-Fe/Fe₅C₂/NG-700 may be attributed to the relatively low conductivity resulting from the low graphitization degree as revealed by Raman spectra (Figure S12, Supporting Information). Whereas for GL-Fe/Fe₅C₂/NG-900, the leaching of active N species as detected by XPS (Figure S4, Supporting Information) at high temperature may be the main reason for the inferior ORR performance. Most importantly, the ORR performance of

the present GL-Fe/Fe₅C₂/NG-800 catalyst is attractive among various carbon or iron carbide-based electrocatalysts (Table S1, Supporting Information). Rotating ring-disk electrode (RRDE) results (Figure 5d) show that the calculated yield of H₂O₂ measured with the GL-Fe/Fe₅C₂/NG-800 catalyst is below 1.8% (calculated by Equation (3)) at the potential ranging from 0.2 to 0.8 V. They correspond to high electron transfer numbers of 3.96–4.00 (calculated by Equation (4)), similar to that of commercial Pt/C. Notably, these results are consistent with the K–L plot obtained from the RDE results, further verifying the four-electron pathway of the ORR reaction. Besides the high ORR activity, the possible fuel crossover effect and long-term stability are also quite important. When 50 mL of methanol is introduced into the O₂-saturated electrolyte, the current density of Pt/C decreases drastically, while GL-Fe/Fe₅C₂/NG-800 is not so sensitive to methanol (Figure 5e), suggesting the strong tolerance of GL-Fe/Fe₅C₂/NG-800 to crossover effect. The durability of GL-Fe/Fe₅C₂/NG-800 and commercial Pt/C is also evaluated through chronoamperometric measurements (Figure 5f). After the durability test for 15 h, about 92% of the initial current density can be maintained, compared to 63% for Pt/C, suggesting the excellent stability of GL-Fe/Fe₅C₂/NG-800. Moreover, the structure of GL-Fe/Fe₅C₂/NG-800 can be well preserved after the stability test (Figure S13, Supporting Information).

The effect of the catalyst mass loading on the ORR performance is investigated through LSV measurement and the optimal mass loading is determined to be 0.15 mg cm⁻² (Figure S14, Supporting Information). We have also studied the effect of mass ratio of ferrocene to g-C₃N₄ on the ORR performance. The samples with ferrocene to g-C₃N₄ ratios of 2:1 and 0.5:1 are also synthesized and denoted as

GL-Fe/Fe₅C₂/NG-800-2 and GL-Fe/Fe₅C₂/NG-800-0.5, respectively. The GL-Fe/Fe₅C₂/NG-800-2 and GL-Fe/Fe₅C₂/NG-800-0.5 exhibit similar composition and morphology to those of GL-Fe/Fe₅C₂/NG-800 (Figures S15 and S16, Supporting Information). In addition, NG can be obtained without adding ferrocene (Figure S15, Supporting Information). All the samples with different mass ratios of ferrocene to g-C₃N₄ show better ORR performance than NG (Figure S17, Supporting Information). The GL-Fe/Fe₅C₂/NG-800 with a ferrocene to g-C₃N₄ ratio of 1:1 displays the best ORR performance. The ORR performance of the GL-Fe/Fe₅C₂/NG-800 is also better than that of the reported CNT-supported Fe₅C₂ nanoparticles without the outer carbon layer,^[28] highlighting the synergistic effect between the N-doped graphene nanosheets and graphene layers-wrapped Fe₅C₂ nanoparticles. In addition, the GL-Fe/Fe₅C₂/NG-800 also exhibits good ORR performance in acidic solution (Figure S18, Supporting Information), which is comparable to many reported metal/carbon-based electrocatalysts (Table S2, Supporting Information). To investigate the possible active sites, Mössbauer effect measurement is carried out to further identify the iron species in the GL-Fe/Fe₅C₂/NG-800. The spectra can be deconvoluted into one singlet and four sextets (Figure S19, Supporting Information). The assignment of the singlet and four sextets to specific Fe species and the related parameters are summarized in Table S3 (Supporting Information). Fe and Fe₅C₂ are the main Fe species in the GL-Fe/Fe₅C₂/NG-800, while no Fe-N₄ species can be detected,^[47–49] which suggests that Fe and Fe₅C₂ might be the main active centers for ORR.

On the basis of the structural and compositional characterization results, it is believed that five important aspects may be responsible for the superior ORR activity and stability. 1) The high specific surface area of the nanocomposites (856 m² g⁻¹) ensures sufficient active sites for electrochemical reactions and facilitates transport of ORR-relevant species. 2) The high percentage of nitrogen doped into the graphene nanosheets can promote O₂ adsorption.^[50,51] 3) The Fe/Fe₅C₂ nanoparticles wrapped in the graphene layers are more electrochemically active for ORR.^[18,27] 4) The graphene layers could effectively suppress the dissolution and agglomeration of iron-rich nanoparticles thus promising good electrochemical activity and stability. 5) The synergistic effect between the N-doped graphene nanosheets and encapsulated Fe/Fe₅C₂ nanoparticles may also contribute to excellent ORR performance. Overall, the excellent electrocatalytic activity, long-term durability, and methanol tolerance ability of NG-Fe/Fe₅C₂/NG-800 make it a promising highly efficient electrocatalyst for ORR.

In summary, we have developed a high-performance ORR electrocatalyst consisting of graphene layers-wrapped Fe/Fe₅C₂ nanoparticles supported on N-doped graphene nanosheets via a facile solid-state reaction of g-C₃N₄ with ferrocene. The reaction mechanism between g-C₃N₄ and ferrocene is carefully investigated. The optimized NG-Fe/Fe₅C₂/NG-800 electrocatalyst exhibits ORR performance superior to commercial Pt/C catalyst, including pronounced activity, remarkable durability, and complete resistance to methanol crossover, making it an excellent nonprecious metal catalyst. The as-demonstrated facile synthetic strategy and proposed reaction mechanism may open a new avenue for developing N-doped graphene-based electrocatalysts for a variety of energy applications.

Experimental Section

Synthesis of Bulk g-C₃N₄: The g-C₃N₄ was prepared according to a previous work by thermal polymerization of melamine.^[9] In a typical synthesis, 10 g of melamine was placed in a ceramic boat with a cover and then heated to 550 °C with a ramp rate of 5 °C min⁻¹ in air and maintained at this temperature for 4 h. Finally, the yellow powder was collected for further use after the furnace cooling down to room temperature.

Synthesis of GL-Fe/Fe₅C₂/NG Electrocatalysts: In a typical synthesis, 0.2 g of as-prepared g-C₃N₄ and 0.2 g of ferrocene were mixed homogeneously by grinding for at least 30 min. Then the mixture was poured into a homemade quartz capsule and pyrolyzed at 800 °C for 2 h with a heating speed of 10 °C min⁻¹ in N₂ atmosphere. To remove unstable and ORR-nonreactive phase, the pyrolyzed black powder was preleached in 1.0 M H₂SO₄ solution for 18 h. The product was collected by centrifugation, repeatedly washed with DI water and ethanol for 10 times, and then dried at 80 °C. Finally, the preleached sample was pyrolyzed for the second time in N₂ atmosphere at the same temperature as the first pyrolysis progress for 2 h to obtain the final electrocatalyst. Before each pyrolysis process, high purity N₂ was bubbled into the tube furnace for at least 1 h. In order to understand the formation mechanism of GL-Fe/Fe₅C₂/NG, the samples obtained at different heating temperatures were investigated. Additionally, the effect of the mass ratio of ferrocene to g-C₃N₄ on the ORR performance was also investigated. The mass of ferrocene was varied from 0.1 to 0.4 g, while the mass of the g-C₃N₄ was fixed at 0.2 g. The synthesis procedure was similar to that of GL-Fe/Fe₅C₂/NG-800. And pure NG was obtained without the addition of ferrocene.

Materials Characterization: The crystalline phase was analyzed by XRD measurements with a Philips PW3040/60 X-ray diffractometer using Cu-K α X-ray source ($\lambda = 0.15406$ nm) radiation at a scanning rate of 0.06 s⁻¹. The tube voltage and current are 40 kV and 40 mA, respectively. The morphology was observed by SEM with a Hitachi S-4800 scanning electron microanalyzer with an accelerating voltage of 15 kV. The samples were prepared by dispersing the products in ethanol and dropped on silicon chip for observation. Microstructures were further characterized by TEM and HRTEM at 200 kV with a JEM-2100F field emission TEM. The surface composition of the samples was analyzed through XPS, using an ESCALab MKII X-ray photoelectron spectrometer with Mg K α X-ray as the excitation source. For TEM measurements, samples were prepared by dispersing the products in ethanol and placing several drops of the suspension on holey carbon net supported on copper grid. N₂ sorption isotherms were obtained at 77 K on a Micrometrics ASAP 2020 surface area and porosity analyzer after the sample had been degassed in vacuum at 200 °C for 4 h. FT-IR was carried out on a Nicolet 5700 FT-IR Spectrometer using the KBr pellet method. The ⁵⁷Fe Mössbauer spectra were recorded using a Topologic 500 A spectrometer and a proportional counter at room temperature. ⁵⁷Co(Rh) moving in a constant acceleration mode was used as radioactive source. All the isomer shift values were reported against the center of a room temperature spectrum recorded for a foil of α -Fe. Samples were protected by Ar during the Mössbauer measurements.

Electrochemical Measurements: The ORR performance was evaluated in a conventional three-electrode cell with a saturated calomel electrode (SCE, saturated KCl) and a Pt foil counter electrode at room temperature using WaveDriver 20 bipotentiostat (Pine Instrument Company, USA). All potentials in this study were converted to the RHE reference scale as follows: $E_{(\text{RHE})} = E_{(\text{SCE})} + 0.059 \times \text{pH} + 0.241$. The electrolyte was 0.1 M KOH solution. An RDE with a glass carbon disk (5 mm in diameter) and an RRDE with a Pt ring (6.5 mm in inner diameter and 8.5 mm in outer diameter) and glass carbon disk (5.5 mm in diameter) coated with catalyst film were used as the working electrodes. For the catalyst ink, 3 mg of the catalyst was dispersed in 920 μL of ethanol and 80 μL of 5% Nafion solution. The mixture was then sonicated for 30 min to obtain a uniform suspension. Then a certain volume of catalyst ink was pipetted on the glass carbon substrate, giving a catalyst loading of 0.15 mg cm⁻² for all samples including commercial Pt/C (20 wt% on carbon black, Alfa

Aesar). Before tests, the electrolyte solution was saturated with O₂ by bubbling O₂ into the cell for 30 min. CV or LSV tests were conducted in O₂- and N₂-saturated electrolyte from 0 to 1.2 V versus RHE with a sweep rate of 20 mV s⁻¹. RDE tests were carried out in O₂-saturated electrolyte with a scan rate of 10 mV s⁻¹ at different rotation speeds from 1.2 to 0 V versus RHE. The fuel crossover effect tests were evaluated by chronoamperometry at the potential of 0.6 V versus RHE by RDE tests with a rotation speed of 1600 rpm with introducing 50 mL of methanol into 150 mL of 0.1 M KOH solution. The apparent electron transfer number was calculated by the K-L equation at various potentials as follows:

$$\frac{1}{j} = \frac{1}{j_L} + \frac{1}{j_K} = \frac{1}{B\omega^{1/2}} + \frac{1}{j_K} \quad (1)$$

$$B = 0.2nFAC_0D_0^{2/3}\nu^{-1/6} \quad (2)$$

where j is the measured current density, j_K and j_L are the kinetic and limiting current densities, respectively, ω is the rotating speed, n is the electron transfer number, F is the Faraday constant (96485 C mol⁻¹), C_0 is the bulk concentration of O₂ (1.2 × 10⁻³ mol L⁻¹), D_0 is the diffusion coefficient of O₂ (1.9 × 10⁻⁵ cm² s⁻¹), and ν is the kinematic viscosity of the electrolyte (0.01 cm² s⁻¹).

RRDE measurements were performed at the voltage range from 0 to 1.2 V versus RHE in O₂-saturated electrolyte at a rotation speed of 1600 rpm with a scan rate of 10 mV s⁻¹. And the Pt ring potential with the collection efficiency of 0.37 provided by the manufacturer was set at 1.5 V. The yield of H₂O₂ and the electron transfer number could be determined by the following equation

$$\text{H}_2\text{O}_2\% = 200 \frac{I_r/N}{I_d + I_r/N} \quad (3)$$

$$n = 4 \frac{I_d}{I_d + I_r/N} \quad (4)$$

where I_d is the disk current, I_r is the ring current, and N is the current collection efficiency of the Pt ring, which was 0.37, provided by the manufacturer.

The ECSA was determined through Equation (5), where the double layer capacitance (C_{dl}) value was estimated by the linear slope of the fitted line which was plotted by capacitive currents versus scan rates, and the C_s value was adopted as ≈0.04 mF cm⁻².^[52]

$$\text{ECSA} = \frac{C_{dl}}{C_s} \quad (5)$$

Supporting Information

Supporting Information is available from the Wiley Online Library or from the author.

Acknowledgements

E.H. and X.Y. contributed equally to this work. Financial supports from the Natural Science Foundation of China (21671173, 61674166), Zhejiang Provincial Natural Science Foundation of China (LR14B010001), and the Zhejiang Provincial Public Welfare Project (2016C31015) are gratefully acknowledged.

Conflict of Interest

The authors declare no conflict of interest.

Keywords

graphene, iron carbides, nanoparticles, oxygen reduction reaction

Received: September 7, 2017

Revised: October 3, 2017

Published online: December 18, 2017

- [1] M. K. Debe, *Nature* **2012**, *486*, 43.
- [2] P. G. Bruce, S. A. Freunberger, L. J. Hardwick, J.-M. Tarascon, *Nat. Mater.* **2012**, *11*, 19.
- [3] B. Y. Xia, Y. Yan, N. Li, H. B. Wu, X. W. Lou, X. Wang, *Nat. Energy* **2016**, *1*, 15006.
- [4] M. Lefèvre, E. Proietti, F. Jaouen, J.-P. Dodelet, *Science* **2009**, *324*, 71.
- [5] R. F. Zhou, S. Z. Qiao, *Chem. Commun.* **2015**, *51*, 7516.
- [6] R. F. Zhou, Y. Zheng, M. Jaroniec, S. Z. Qiao, *ACS Catal.* **2016**, *6*, 4720.
- [7] C. Meng, T. Ling, T. Y. Ma, H. Wang, Z. P. Hu, Y. Zhou, J. Mao, X. W. Du, S. Z. Qiao, *Adv. Mater.* **2017**, *29*, 1604607.
- [8] J. Wang, K. Wang, F.-B. Wang, X.-H. Xia, *Nat. Commun.* **2014**, *5*, 5285.
- [9] J. Liang, R. F. Zhou, X. M. Chen, Y. H. Tang, S. Z. Qiao, *Adv. Mater.* **2014**, *26*, 6074.
- [10] Y. Nie, L. Li, Z. Wei, *Chem. Soc. Rev.* **2015**, *44*, 2168.
- [11] J. Yang, H. Sun, H. Liang, H. Ji, L. Song, C. Gao, H. Xu, *Adv. Mater.* **2016**, *28*, 4606.
- [12] W. Ding, L. Li, K. Xiong, Y. Wang, W. Li, Y. Nie, S. Chen, X. Qi, Z. Wei, *J. Am. Chem. Soc.* **2015**, *137*, 5414.
- [13] H. Hu, L. Han, M. Yu, Z. Wang, X. W. Lou, *Energy Environ. Sci.* **2016**, *9*, 107.
- [14] H.-W. Liang, W. Wei, Z.-S. Wu, X. Feng, K. Müllen, *J. Am. Chem. Soc.* **2013**, *135*, 16002.
- [15] G. Wu, K. L. More, C. M. Johnston, P. Zelenay, *Science* **2011**, *332*, 443.
- [16] C. Li, X. Han, F. Cheng, Y. Hu, C. Chen, J. Chen, *Nat. Commun.* **2015**, *6*, 7345.
- [17] Z.-Y. Wu, X.-X. Xu, B.-C. Hu, H.-W. Liang, Y. Lin, L.-F. Chen, S.-H. Yu, *Angew. Chem. Int. Ed.* **2015**, *127*, 8297.
- [18] Y. Hu, J. O. Jensen, W. Zhang, L. N. Cleemann, W. Xing, N. J. Bjerrum, Q. Li, *Angew. Chem. Int. Ed.* **2014**, *53*, 3675.
- [19] L. Dai, Y. Xue, L. Qu, H.-J. Choi, J.-B. Baek, *Chem. Rev.* **2015**, *115*, 4823.
- [20] K. Qu, Y. Zheng, S. Dai, S. Z. Qiao, *Nano Energy* **2016**, *19*, 373.
- [21] Y. Zheng, Y. Jiao, L. Ge, M. Jaroniec, S. Z. Qiao, *Angew. Chem. Int. Ed.* **2013**, *125*, 3192.
- [22] T.-N. Ye, L.-B. Lv, X.-H. Li, M. Xu, J.-S. Chen, *Angew. Chem. Int. Ed.* **2014**, *53*, 6905.
- [23] L.-B. Lv, T.-N. Ye, L.-H. Gong, K.-X. Wang, J. Su, X.-H. Li, J.-S. Chen, *Chem. Mater.* **2015**, *27*, 544.
- [24] B. Y. Guan, L. Yu, X. W. Lou, *Energy Environ. Sci.* **2016**, *9*, 3092.
- [25] Z. Wen, S. Ci, F. Zhang, X. Feng, S. Cui, S. Mao, S. Luo, Z. He, J. Chen, *Adv. Mater.* **2012**, *24*, 1399.
- [26] J. Wei, Y. Liang, Y. Hu, B. Kong, G. P. Simon, J. Zhang, S. P. Jiang, H. Wang, *Angew. Chem. Int. Ed.* **2016**, *128*, 1377.
- [27] M. Xiao, J. Zhu, L. Feng, C. Liu, W. Xing, *Adv. Mater.* **2015**, *27*, 2521.
- [28] V. Vij, J. N. Tiwari, W.-G. Lee, T. Yoon, K. S. Kim, *Sci. Rep.* **2016**, *6*, 20132.
- [29] P. Niu, L. Zhang, G. Liu, H.-M. Cheng, *Adv. Funct. Mater.* **2012**, *22*, 4763.
- [30] J. Liang, Y. Zheng, J. Chen, J. Liu, D. Hulicova-Jurcakova, M. Jaroniec, S. Z. Qiao, *Angew. Chem. Int. Ed.* **2012**, *51*, 3892.

- [31] T. Y. Ma, S. Dai, M. Jaroniec, S. Z. Qiao, *Angew. Chem. Int. Ed.* **2014**, *53*, 7281.
- [32] A. M. El-Sawy, I. M. Mosa, D. Su, C. J. Guild, S. Khalid, R. Joesten, J. F. Rusling, S. L. Suib, *Adv. Energy Mater.* **2016**, *6*, 1501966.
- [33] X. Zhang, X. Xie, H. Wang, J. Zhang, B. Pan, Y. Xie, *J. Am. Chem. Soc.* **2013**, *135*, 18.
- [34] Q. Han, B. Wang, J. Gao, Z. Cheng, Y. Zhao, Z. Zhang, L. Qu, *ACS Nano* **2016**, *10*, 2745.
- [35] P. Niu, L.-C. Yin, Y.-Q. Yang, G. Liu, H.-M. Cheng, *Adv. Mater.* **2014**, *26*, 8046.
- [36] H. Yu, L. Shang, T. Bian, R. Shi, G. I. N. Waterhouse, Y. Zhao, C. Zhou, L.-Z. Wu, C.-H. Tung, T. Zhang, *Adv. Mater.* **2016**, *28*, 5080.
- [37] X.-H. Li, S. Kurasch, U. Kaiser, M. Antonietti, *Angew. Chem. Int. Ed.* **2012**, *51*, 9689.
- [38] J. Li, Y. Zhang, X. Zhang, J. Han, Y. Wang, L. Gu, Z. Zhang, X. Wang, J. Jian, P. Xu, B. Song, *ACS Appl. Mater. Interfaces* **2015**, *7*, 19626.
- [39] Y. Liu, H. Jiang, Y. Zhu, X. Yang, C. Li, *J. Mater. Chem. A* **2016**, *4*, 1694.
- [40] Y.-Z. Chen, C. Wang, Z.-Y. Wu, Y. Xiong, Q. Xu, S.-H. Yu, H.-L. Jiang, *Adv. Mater.* **2015**, *27*, 5010.
- [41] W. Niu, L. Li, X. Liu, N. Wang, J. Liu, W. Zhou, Z. Tang, S. Chen, *J. Am. Chem. Soc.* **2015**, *137*, 5555.
- [42] W.-J. Jiang, L. Gu, L. Li, Y. Zhang, X. Zhang, L.-J. Zhang, J.-Q. Wang, J.-S. Hu, Z. Wei, L.-J. Wan, *J. Am. Chem. Soc.* **2016**, *138*, 3570.
- [43] Y. Liu, Y. Hu, M. J. Zhou, H. S. Qian, X. Hu, *Appl. Catal., B* **2012**, *125*, 425.
- [44] Y. Hu, J. O. Jensen, W. Zhang, Y. Huang, L. N. Cleemann, W. Xing, N. J. Bjerrum, Q. Li, *ChemSusChem* **2014**, *7*, 2099.
- [45] L. M. Dyagileva, V. P. Mar'in, E. I. Tsyganova, G. A. Razuvaev, *J. Organomet. Chem.* **1979**, *175*, 63.
- [46] Y. Hu, J. O. Jensen, W. Zhang, S. Martin, R. Chenitz, C. Pan, W. Xing, N. J. Bjerrum, Q. Li, *J. Mater. Chem. A* **2015**, *3*, 1752.
- [47] U. I. Kramm, M. Lefèvre, N. Larouche, D. Schmeisser, J.-P. Dodelet, *J. Am. Chem. Soc.* **2014**, *136*, 978.
- [48] U. I. Kramm, I. Abs-Wurmbach, I. Herrmann-Geppert, J. Radnik, S. Fiechter, P. Bogdanoff, *J. Electrochem. Soc.* **2011**, *158*, B69.
- [49] A. L. Bouwkamp-Wijnoltz, W. Visscher, J. A. R. van Veen, E. Boellaard, A. M. van der Kraan, S. C. Tang, *J. Phys. Chem. B* **2002**, *106*, 12993.
- [50] X. Wang, P. Zhang, W. Wang, X. Lei, H. Yang, *Chem.-Eur. J.* **2016**, *22*, 4863.
- [51] W. Yang, X. Liu, X. Yue, J. Jia, S. Guo, *J. Am. Chem. Soc.* **2015**, *137*, 1436.
- [52] C. C. L. McCrory, S. Jung, J. C. Peters, T. F. Jaramillo, *J. Am. Chem. Soc.* **2013**, *135*, 16977.